ChemComm

COMMUNICATION

View Article Online
View Journal | View Issue

Cite this: *Chem. Commun.*, 2016, **52**, 3300

Received 6th November 2015,
Accepted 20th January 2016

DOI: 10.1039/c5cc09165a

www.rsc.org/chemcomm

In situ atomic scale visualization of surface kinetics driven dynamics of oxide growth on a Ni–Cr surface†

Langli Luo,[a] Lianfeng Zou,[b] Daniel K. Schreiber,[c] Matthew J. Olszta,[c] Donald R. Baer,[a] Stephen M. Bruemmer,[c] Guangwen Zhou*[b] and Chong-Min Wang*[a]

We report the *in situ* atomic-scale visualization of the dynamic three-dimensional growth of NiO during the initial oxidation of Ni–10at%Cr using environmental transmission electron microscopy. A step-by-step adatom growth mechanism in 3D is observed and a change in the surface planes of growing oxide islands can be induced by local surface kinetic variations.

The interaction of oxygen with alloy surfaces is of great interest to a wide range of technological applications including passivation of metals,[1–3] heterogeneous catalysis[4–6] and failure of semiconductor devices.[7,8] However, many fundamental questions persist especially in the initial stages of oxidation. Among them, the atomic mechanism underlying the 3D growth of oxide islands beyond a few layers is largely unknown although surface science studies have provided tremendous information on oxygen adsorption induced metal surface reconstructions.[9–11] The early stages of metal oxidation generally involve the nucleation and growth of 3D oxide islands before steady-state oxidation begins.[12–16] Early oxidation stages for alloys are complicated by the nucleation and growth of different oxide phases, where more than one element can be oxidized simultaneously.[17,18] From the practical point of view, the early-stage oxidation behavior can exert a strong influence on the microstructure evolution of the oxide film in the later stages of the oxidation and thus the kinetics of the steady-state oxidation.

A step-edge induced oxide growth as a result of direct interaction of oxygen gas and the metal surface has been reported on Cu surfaces.[19] Different from the long-held oxidation model of the solid–solid transformation,[20–24] the presence of surface steps facilitates oxide formation without involving oxygen subsurface incorporation. The initial oxide film can grow from a 2D wetting-layer to 3D islands by overcoming a critical thickness, which is similar to the Stranski–Krastanov (SK) mode of thin film growth.[25,26] The 3D islands with a thickness of a few atomic layers are usually not well faceted while several compact island shapes – including squares, triangles, hexagons and round shapes – are prevalently found during the early stages of metal and alloy oxidation.[13] To understand how these different shapes have developed, we need to know the underlying mechanism for 3D oxide growth. Ni–Cr is a model alloy system for developing oxidation-resistive alloys.[27] Since both Ni and Cr can be oxidized, the growth of initial oxides is of great importance in determining the microstructure of the oxide scale toward effective passivation of the alloy. Herein, we employ *in situ* environmental transmission electron microscopy (ETEM) to monitor the initial oxide growth on a Ni–10at%Cr surface at the atomic scale in real time. We observe that in this process NiO crystals nucleate and grow epitaxially on the Ni–Cr surface first, and then it proceeds through step-by-step adatom mechanisms sustained by surface diffusion of Ni and O atoms. The surface planes of the oxide islands can be changed upon the surface kinetic variation. No Cr_2O_3 phase has been found during the initial oxidation process ($\sim$5 min). These results demonstrate that the surface diffusion determines the morphology and growth kinetics of oxide islands during the initial oxidation of Ni–Cr alloy.

The oxidation experiments were carried out in an environmental TEM (FEI Titan® 80–300) equipped with an objective-lens aberration corrector. The single crystal Ni–10at%Cr(100) thin film of $\sim$40 nm was grown on a NaCl(100) substrate by e-beam evaporation. The alloy film was removed from the substrate by suspending in the deionized water, then washed (in acetone and methanol) and mounted on the TEM grid. The Ni–Cr films were annealed using the Gatan® 652 double-tilt heating holder at 450 °C with the flow of H_2 gas to remove native oxides. *In situ* TEM observations were made in both the planar view on the (100) surface and the cross-sectional view on the ⟨110⟩ edges of the Ni–10at%Cr(100) film oxidized at 450 °C at an oxygen partial pressure $pO_2 = 3 \times 10^{-6}$ mbar unless otherwise specified.

Fig. 1A–C depicts the general process of oxide growth on the Ni–10at%Cr(100) film for the first few minutes, which proceeds

[a] *Environmental Molecular Sciences Laboratory, Pacific Northwest National Laboratory, Richland, WA 99352, USA. E-mail: Chongmin.wang@pnnl.gov*
[b] *Department of Mechanical Engineering & Multidisciplinary Program in Materials Science and Engineering, State University of New York, Binghamton, NY13902, USA. E-mail: gzhou@binghamton.edu*
[c] *Energy and Environment Directorate, Pacific Northwest National Laboratory, Richland, WA 99352, USA*

† Electronic supplementary information (ESI) available: For ESI and *in situ* videos. See DOI: 10.1039/c5cc09165a

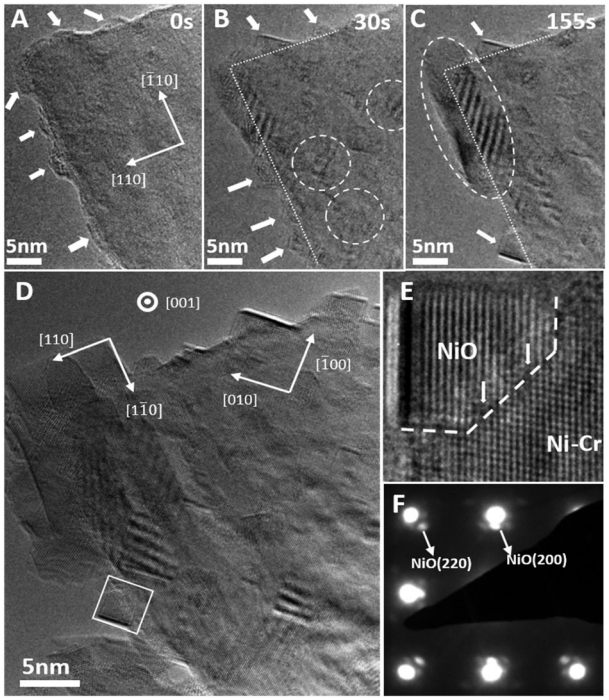

Fig. 1 (A–C) *In situ* TEM images of nucleation and growth of NiO on two ⟨110⟩ edges of Ni–10at%Cr(100) during the oxidation at 450 °C and pO_2 = 3 × 10^{-6} mbar (see *in situ* TEM Movie S1 in the ESI†). (D) Oxidized alloy surface after 363 s shows cubic oxide islands exposing only ⟨100⟩ or ⟨110⟩ surfaces. (E) The HRTEM image of an enlarged area from (D) shows the epitaxial relationship between the oxide and the alloy substrate, the interface is indicated as a white dotted line and white arrows show two dislocations. (F) Selected-area electron diffraction pattern of the oxidized alloy surface shows the epitaxial relationship between the oxide and the alloy.

through oxide islands along the film edges and on the film surface. Immediately after the introduction of oxygen gas, oxide nucleation occurs along the two ⟨011⟩ edges of the alloy film indicated by arrows in Fig. 1A. These initial oxide films do not show any strong diffraction contrast of lattices, indicating that they may not have well-ordered crystal structures as adjacent alloy films. They can experience oscillatory growth due to the presence of surface steps leading to metastable atomic structures.[28] Upon continued oxidation, all of the edge-on oxide (white arrows) grows into stable 3D oxide with clear facets after 30 s, as seen in Fig. 1B. Simultaneously, oxidation proceeds along the entire planar surface area of the alloy film, as evidenced by the Moiré fringes (dashed-line circles) caused by overlapping NiO and Ni–Cr lattices. After 155 s, the lateral dimensions of the NiO oxide reach 5 nm and the corner oxide island (dashed-line ellipse) with the ⟨110⟩ surface planes outgrow the other two oxide islands with the ⟨100⟩ surface planes (up and bottom arrows) seen in Fig. 1C. The edges of the alloy sample are indicated by white-dashed lines in Fig. 1B and C. Fig. 1D shows a high-resolution (HR) TEM image of this Ni–10at%Cr(100) thin film oxidized for 363 s. It can be seen that the two ⟨110⟩ edges and the planar surface area of the film are fully covered with several NiO islands with either (100) or (011) surfaces. The enlarged HRTEM image in Fig. 1E shows a NiO island grown on the Ni–Cr(011) surface with an epitaxial relationship of (001)NiO‖(001)Ni–Cr and [011]NiO‖[011]Ni–Cr. The interface between the NiO island and the metal alloy substrate is depicted by a white dotted line, and two white arrows indicate the locations of misfit dislocations caused by their lattice mismatch. The NiO phase and cube-on-cube epitaxy were further confirmed by the selected-area electron diffraction (SAED) pattern in Fig. 1F. No additional reflections from other oxide phases (*e.g.* $NiCr_2O_4$ or Cr_2O_3) were observed and the additional satellite spots are caused by double-diffraction. Although it is possible that Cr forms oxides without well-ordered crystal structures resulting in no diffraction spots in the SAED pattern, all of the oxide islands emerged on the alloy surface show the epitaxial NiO phase in Fig. 1D. Cross-sectional TEM imaging of a similar sample with a longer oxidation time revealed Cr-rich oxide at the interface between outward growing NiO and the metal alloy, suggesting that Cr is also oxidized but does not inhibit NiO formation in this initial stage. This delayed formation of Cr-based oxides has been reported for both Fe–Cr and Ni–Cr alloys,[2] *i.e.*, the alloys at a lower concentration (<15%) of Cr show no Cr_2O_3 phase in the first few minutes while the Cr_2O_3 phase is always present in the alloy at a higher (~30%) Cr concentration. The absence of Cr-based oxides during the initial oxidation of the alloy with a low Cr concentration is largely because the kinetically favored NiO formation consumes all the oxygen atoms on the surface in our test conditions resulting in trace amounts or no Cr based oxide formation. From these observations, it is apparent that the initial oxidation of Ni–Cr film is dominated by the epitaxial growth of NiO rather than Cr oxide. As the oxide island growth continues, cubic island morphologies develop along the alloy surface. The 3D growth of oxide islands results from the increasing strain energy caused by a lattice mismatch between NiO and Ni–Cr in the system. According to Vegard's law, for a solid solution Ni–10at%Cr alloy with the same face-centered cubic (fcc) structure as pure Ni, the lattice constant is calculated as $a_{Ni-10at\%Cr} = (1 - 0.1)a_{Ni} + 0.1a_{Cr}$ = 3.456 Å. The natural lattice misfit, $f = (a_{NiO} - a_{Ni-10at\%Cr})/a_{NiO}$, between Ni–Cr and NiO is ~17.1%. As seen in Fig. 1E, this large lattice misfit is accommodated by the presence of misfit dislocations, *i.e.*, dislocations appear for every 6 atomic layers of the NiO lattice, which results in a reduced lattice mismatch between the oxide and the alloy substrate. The measured lattice misfit between Ni–Cr (measured as 3.514 Å) and NiO (measured as 4.02 Å) is ~14.3%. Although the grown NiO is still strained by ~2% compared with the natural lattice space of NiO ~4.17 Å, the relaxation of a large lattice misfit makes the 3D growth of oxide islands thermodynamically favorable over a 2D epitaxial layer growth because the reduction in the epitaxial strain energy outweighs the increase in island surface energy.

Fig. 2 depicts the dynamic atomistic process of NiO island growth on the Ni–Cr(100) surface through a series of time-resolved HRTEM images. In Fig. 2A, three oxide islands are present on the Ni–Cr(100) surface as shown clearly by the Moiré fringes. The following images in Fig. 2B–G focus on the [100] edge of the oxide island located at the center (indicated by the white box in Fig. 2A). The *in situ* TEM images show that the oxide grows through a layer-by-layer mode by consuming the adjacent stepped alloy surface. Initially, the growth front of the new oxide layer (indicated by the white arrow in Fig. 2B) propagates from the right to the left side. After 8 s (Fig. 2C), it has grown ~3.1 nm laterally, corresponding to ~15 atomic columns (the lattice distance for NiO(200) planes is 2.08 Å) shown in Fig. 2C. At the same time, the upper terrace of the stepped alloy surface on

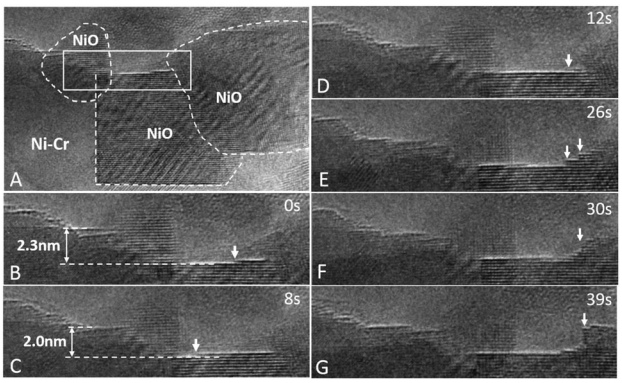

Fig. 2 (A) HRTEM image of three NiO islands grown on Ni–10at%Cr(100) during the oxidation at 450 °C and $pO_2 = 3 \times 10^{-6}$ mbar. (B–G) Time-resolved HRTEM images of NiO islands growth under the above conditions (see *in situ* TEM Movie S2 in the ESI†).

the left decreases its height from 2.3 nm to 2.0 nm indicating that Ni atoms in this region are consumed for the oxide growth, possibly through atom detachment from the stepped surface. Within another 4 s, a second oxide layer has grown as seen in Fig. 2D. These *in situ* TEM images clearly show that the oxide island grows layer by layer *via* an adatom process, which involves the preferential formation of a new oxide at the step-edge and the step-edge moves laterally as the oxidation proceeds. It is natural to expect that step edges are thermodynamically favoured sites for oxide formation because they lower the system free energy. But it is also noted that because Ni atoms have to diffuse to the reaction front on the oxide surface to grow an oxide layer, the upper terrace has a shorter diffusion length compared with the lower terrace, which makes it possible to nucleate new oxide on the upper terrace. The interplay of thermodynamic and kinetic factors results in the growth of a new oxide on both upper and lower terraces but the oxide on the upper terrace is always limited by the step-edges as illustrated in Fig. 2E–G, wherein the new oxide layers (indicated by arrows) on the upper terrace cannot cross the existing step-edge leading to the formation of two-atomic-layer and even four-atomic-layer high steps during the oxide growth. This has been observed previously[28] for the oxide formation on Cu surfaces, which is due to oxygen adsorption on the lower terrace along the step-edge, destabilizing the oxide layer formed on the upper terrace. It is also noted that an additional oxide layer propagates from left to right and meets with the growth front of an existing oxide layer in Fig. 2F, which indicates that the new oxide growth on the lower terrace is possible and follows the adatom growth mode.

The layer-by-layer adatom growth mode of oxide islands observed above requires fast surface diffusion of Ni and O atoms to the step-edge growth front. When the dimensions of the oxide islands are small and the alloy surface is not fully covered with oxides, the diffusion of Ni atoms over the surface of oxide islands is kinetically more favorable than bulk diffusion through oxide islands. While O molecules directly impinge, dissociate and diffuse on the entire sample surface, the consumption of Ni atoms from the alloy was observed directly through the decreasing step height and changing step edges as seen in Fig. 2. Further evidence on a larger length scale can be seen in the time-resolved bright-field TEM images in Fig. S1 (ESI†). The increasing area of white contrast with the oxidation time clearly shows that the consumption of the Ni–Cr alloy during oxidation proceeds in a fashion of layer-by-layer peeling of atoms along the ⟨100⟩ directions. Taken together, these observations clearly demonstrate that the initial oxidation of Ni–10at%Cr is dominated by surface diffusion of Ni and O atoms.

The equilibrium shapes of crystals are usually related to their surface energies and can be determined by Wulff constructions. The oxidation of metals is a "non-equilibrium" process, which can be a kinetics-dominated process as shown above. Hence, the shapes of the growing oxide islands can be dynamic and sensitive to the changes in kinetic conditions. This metastability is illustrated for NiO by a transition of surface planes from the (100) to (110) surfaces on a small oxide island as seen in a series of time-resolved HRTEM images in Fig. 3. In Fig. 3A, the oxide island has an exposed edge-on (100) surface plane as indicated by the solid white arrow. With time new oxide layers grew from the top-left to the bottom-right of the (100) plane until they intersected the alloy surface. Two step-edges are clearly visible in Fig. 3B after 21 s, indicating that a few atomic layers of oxide have grown onto the NiO(100). Rather than the layer-by-layer growth observed in Fig. 2, the large step height (1–2 nm) here indicates that the step consists of multiple atomic layers. Therefore the propagation of a single-layer step-edge is much slower than the formation of new oxide layers on the upper terrace. At the same time, the upper-most oxide layer consistently stops growing at the step-edges, resulting in the formation of a dome-like new island seen in Fig. 3C. By accumulating new oxide layers on the (100) surface, which are limited by steps, a new (110) surface plane is partially formed where many step-edges meet as seen in Fig. 2D. This new (110) plane meets the pre-existing (100) step resulting in a new step-edge with a 135° slope, which becomes the new growth front of the oxide layer. In Fig. 3D and E, the new oxide layer grows from the new step-edge to the far end of the new (110) surface as evidenced by the advancement of a step-edge indicated by the white arrows. Through this atomistic route, the new (110) surface plane has completely replaced the original (100) surface plane after 128 s of oxidation as seen in Fig. 3F. This transition of the growing surface planes of the oxide island may stem from locally inhibited diffusion on the (100) surface of the oxide island along with the Ehrlich–Schwoebel (E–S) barrier[29,30] inhibiting crossing of the step-edge. As seen in Fig. 3, a growing NiO island indicated by the dashed-line arrow is visible on the right side of the central oxide island.

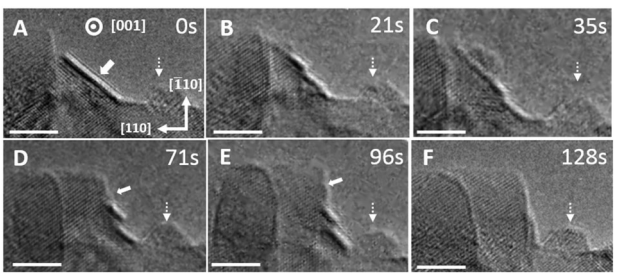

Fig. 3 (A–F) Time-resolved HRTEM images of the (100) surface of one NiO island grown on Ni–10at%Cr(100) during the oxidation at 450 °C and $pO_2 = 3 \times 10^{-6}$ mbar, depicting a transition from the (100) to the (110) surface of the NiO island. The scale bar is 5 nm.

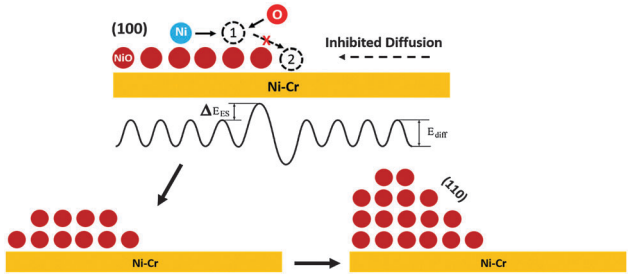

Fig. 4 Schematic of the transition from (100) to (110) surfaces on a NiO island during the oxidation of Ni–10at%Cr alloy. (Upper) Ni atom (blue) diffuses to site 1 to form NiO (brown) with O (red) on the initial NiO layer but cannot diffuse to site 2 on the lower terrace because of the additional E–S barrier. (Lower left) More NiO layers formed on the upper terrace leading to (Lower right) the transition from (100) to (110) surface of NiO. Note that the surface diffusion of Ni and O are inhibited from right indicated as a dashed-line arrow because of the existence of another NiO island on the right (not shown here).

As oxidation proceeds, this oxide island grows and approaches the central oxide island, inhibiting the diffusion of Ni and O atoms nearby. This occurs because each oxide island acts as a sink for the reacting species in a surface diffusion governed oxidation process.[12]

Hence, the growth of two adjacent oxide islands inhibits surface diffusion of the reacting species (Ni and O) in the area between them. Fig. 4 shows the schematic of the (100) → (110) transition for the oxide surface caused by this local kinetic variation. Because of the inhibited surface diffusion of reacting species from the lower terrace (right side), most of Ni atoms diffuse to the upper terrace from the left side (Fig. 4A). For a stepped surface, the E–S barrier is an additional diffusion barrier, encountered by a moving surface atom when crossing an atomic step since it has to pass through the area (steps) with fewer number of nearest neighbors compared with those on the terrace. Hence, Ni atoms have a much larger chance to diffuse to site 1 rather than cross the step-edge to site 2, resulting in the preferential formation of new oxide layers on the upper terrace rather than on the lower terrace (Fig. 4B). While more oxide layers nucleate and grow on the upper layer, layer by layer, step-edges are being created through this process at the same time. These step-edges construct even a larger E–S barrier for atomic diffusion. Eventually, these step-edges line up to form the new (110) surface on the oxide island (Fig. 4C). This illustrates how the surface diffusion controls the growth morphology of oxide islands during initial oxidation of the alloy.

In summary, we have observed the atomistic processes of the 3D growth of oxide islands during the initial stages of Ni–10at%Cr alloy oxidation in real time. Our *in situ* TEM visualization reveals that the oxide growth generally proceeds through an adatom mechanism involving surface diffusion of Ni and O atoms to the growth front. This layer-by-layer growth mode can be altered by variation in local kinetics, *i.e.* limited surface diffusion in the area adjacent to the oxide island. This can lead to a transition from (100) to (110) surface planes of the oxide island, which can be understood through the effect of the E–S barrier. The understanding of the detailed atomistic route for 3D growth of oxide islands on the alloy surface not only provides insight into the effective passivation of the alloy surface but also has a broader impact on controlling the growth of heterogeneous nanostructures on the substrate.

This work was supported by the US Department of Energy (DOE), Office of Basic Energy Sciences, Division of Materials Sciences and Engineering. The work was conducted in the William R. Wiley Environmental Molecular Sciences Laboratory (EMSL), a DOE User Facility operated by Battelle for the DOE Office of Biological and Environmental Research. Pacific Northwest National Laboratory was operated for the DOE under Contract DE-AC06-76RLO 1830. The work of Binghamton University was supported by the U.S. Department of Energy, Office of Basic Energy Sciences, Division of Materials Sciences and Engineering under Award No. DE-FG02-09ER46600.

Notes and references

1 D. L. Douglass, *Corros. Sci.*, 1968, **8**, 665–678.
2 B. Chattopadhyay and G. C. Wood, *J. Electrochem. Soc.*, 1970, **117**, 1163–1171.
3 G. Calvarin, R. Molins and A. M. Huntz, *Oxid. Met.*, 2000, **53**, 25–48.
4 F. Besenbacher, I. Chorkendorff, B. S. Clausen, B. Hammer, A. M. Molenbroek, J. K. Nørskov and I. Stensgaard, *Science*, 1998, **279**, 1913–1915.
5 K.-W. Park, J.-H. Choi, B.-K. Kwon, S.-A. Lee, Y.-E. Sung, H.-Y. Ha, S.-A. Hong, H. Kim and A. Wieckowski, *J. Phys. Chem. B*, 2002, **106**, 1869–1877.
6 E. Nikolla, J. Schwank and S. Linic, *J. Catal.*, 2009, **263**, 220–227.
7 L. Chan, K.-P. Yap, K.-C. Tee, F. S. Ip and W.-B. Loh, *US pat.*, 6100195, 2000.
8 N. L. Michael, C.-U. Kim, P. Gillespie and R. Augur, *Appl. Phys. Lett.*, 2003, **83**, 1959–1961.
9 D. F. Mitchell, P. B. Sewell and M. Cohen, *Surf. Sci.*, 1976, **61**, 355–376.
10 G. Allen, P. Tucker and R. Wild, *Oxid. Met.*, 1979, **13**, 223–236.
11 S. M. Thurgate and P. J. Jennings, *Surf. Sci.*, 1983, **131**, 309–320.
12 J. C. Yang, M. Yeadon, B. Kolasa and J. M. Gibson, *Appl. Phys. Lett.*, 1997, **70**, 3522.
13 G. Zhou and J. C. Yang, *Appl. Surf. Sci.*, 2003, **210**, 165.
14 L. Wang and J. C. Yang, *J. Mater. Res.*, 2005, **20**, 1902–1909.
15 L. Luo, Y. Kang, J. C. Yang, D. Su, E. A. Stach and G. Zhou, *Appl. Phys. Lett.*, 2014, **104**, 121601.
16 L. Luo, Y. Kang, J. C. Yang and G. Zhou, *J. Appl. Phys.*, 2015, **117**, 065305.
17 F. Gesmundo and B. Gleeson, *Oxid. Met.*, 1995, **44**, 211–237.
18 M. P. Brady, I. G. Wright and B. Gleeson, *JOM*, 2000, **52**, 16–21.
19 G. Zhou, L. Luo, L. Li, J. Ciston, E. A. Stach and J. C. Yang, *Phys. Rev. Lett.*, 2012, **109**, 235502.
20 K. R. Lawless, *Rep. Prog. Phys.*, 1974, **37**, 231.
21 M. Todorova, W. X. Li, M. V. Ganduglia-Pirovano, C. Stampfl, K. Reuter and M. Scheffler, *Phys. Rev. Lett.*, 2002, **89**, 096103.
22 J. Gustafson, A. Mikkelsen, M. Borg, E. Lundgren, L. Köhler, G. Kresse, M. Schmid, P. Varga, J. Yuhara, X. Torrelles, C. Quirós and J. N. Andersen, *Phys. Rev. Lett.*, 2004, **92**, 126102.
23 M. Todorova, K. Reuter and M. Scheffler, *Phys. Rev. B: Condens. Matter Mater. Phys.*, 2005, **71**, 195403.
24 U. Starke, M. A. Van Hove and G. A. Somorjai, *Prog. Surf. Sci.*, 1994, **46**, 305–319.
25 Y. W. Mo, D. E. Savage, B. S. Swartzentruber and M. G. Lagally, *Phys. Rev. Lett.*, 1990, **65**, 1020–1023.
26 G. Zhou, L. Luo, L. Li, J. Ciston, E. A. Stach, W. A. Saidi and J. C. JYang, *Chem. Commun.*, 2013, **49**, 10862–10864.
27 B. Chattopadhyay and G. C. Wood, *Oxid. Met.*, 1970, **2**, 373–399.
28 L. Li, L. Luo, J. Ciston, W. A. Saidi, E. A. Stach, J. C. Yang and G. Zhou, *Phys. Rev. Lett.*, 2014, **113**, 136104.
29 R. L. Schwoebel and E. J. Shipsey, *J. Appl. Phys.*, 1966, **37**, 3682–3686.
30 R. L. Schwoebel, *J. Appl. Phys.*, 1969, **40**, 614–618.